CHINA FOUNDRY Research & Development
Vol.16 No.5 September 2019
https://doi.org/10.1007/s41230-019-9072-z

Global heat transfer model and dynamic ray tracing algorithm for complex multiple turbine blades of Ni-based superalloys in directional solidification process

Wen Wang, Jian-xin Zhou, *Zhao Guo, Ya-jun Yin, Xu Shen and Xiao-yuan Ji

State Key Laboratory of Materials Processing and Die &Mould Technology,Huazhong University of Science and Technology, Wuhan 430074, China

Abstract: High-quality solidification microstructure during directional solidification relies on precise temperature gradient control, so accurate calculation of the temperature field is critical. In this study, a 3D transient global heat transfer model of directional solidification by the Bridgman method based on the finite difference method is developed. The radiation heat in this model is calculated by the discrete transfer method, and a modified method of external surface area for irregular geometric models is proposed to reduce the zigzag shape caused by finite difference grids. Considering the radiative heat transfer between any surface elements of all materials in the directional solidification furnace, a dynamic ray tracing algorithm is developed to simulate the entire process of directional solidification. Then, the simulated results are compared with the theoretical results and experimental results, respectively. Finally, based on the present model and method, the simulation program developed is applied to the directional solidification of actual castings. The simulated results are in good agreement with the experimental results, which indicate that the model and method developed in this study is effective and practical.

Key words: radiative heat transfer; ray tracing; turbine blade; directional solidification; numerical simulation

CLC numbers: TG146.1+5/TP391.9 **Document code:** A **Article ID:** 1672-6421(2019)05-326-10

Currently, directional solidification technology is widely used in manufacturing high-performance turbine blades for aero engines [1-4]. By controlling the thermal gradient during the solidification process of molten alloy, the preferential growth of the alloy grain can be promoted in a certain direction. Then the stress perpendicular to the grain growth direction in the blade is weakened or eliminated, thus improving the mechanical properties of the blade. Nevertheless, in the directional solidification furnace, due to the limitations of equipment structure and process conditions, it is difficult to accurately and efficiently control the temperature field of the solidification process by traditional methods.

Over recent decades, with the development of computer technology, numerical simulation has become a powerful tool for predicting the temperature field in directional solidification process. Many efforts have been made to develop the numerical model and solve the heat transfer problems of the directional solidification process.Aiming at the entire process of directional solidification, a transient three-dimensional (3D) finite element model was developed by Thomas and Goettsch to calculate the temperatures [5]. The model can work with the problem of moving boundary very well. Galantucci and Tricarico [6] proposed a simple axisymmetrical thermal model based on the finite-element method (FEM) considering the influence of different working parameters on the simulation results. With this model, thermal gradients can be quickly calculated and used to optimize process parameters. For both directional solidification methods by the conventional Bridgman and liquid metal cooling (LMC) techniques, Elliott and Pollock [7] presented a two-dimensional cropped model, which was used to evaluate and analyze the unique limiting heat-transfer step of each process. According to the simulation results, the process conditions of heat transfer can be optimized reasonably. Miller [8] adopted a 3D finite-element solidification model to investigate the heat extraction of directional solidification by the LMC technique. It is found that an abrupt change in the local temperature field can lead to the growth of grains deviating from the heat flow direction. On the other hand, based on the finite difference method (FDM), Yu J, et al.[9] developed a 3D mathematical model for the simulation of single

***Zhao Guo**

Male, born in 1988, Ph.D. Candidate. Research interests: numerical simulation of material processing process.

E-mail: zg2014@hust.edu.cn

Received: 2019-05-28; Accepted: 2019-07-18

crystal investment castings. In this model, the Monte Carlo method is used to reduce the computation of the view factor of characteristic rays. The simulated results agree well with the experimental results. Subsequently, Yan X W, et al. [10] applied this numerical model and method to the multi-scale simulation of a single crystal hollow turbine blade manufactured by LMC process. It was found that the mushy zone might be convex and ahead of the ceramic beads at a lower withdrawal rate.

As mentioned above, the huge amount of calculation is still one of the main factors limiting the numerical simulation of the directional solidification process [6, 8]. In addition, the radiant heat transfer between other materials has received only limited attention. To further improve the accuracy of numerical simulation for complex multiple turbine blades of Ni-based superalloys in the directional solidification process, a 3D transient global heat transfer model of directional solidification by the Bridgman method based on FDM was developed. The radiation heat in this model was calculated by the Discrete Transfer Method (DTM), and an external surface area modified method for irregular geometric models was proposed to reduce the zigzag shape caused by finite difference grids. Considering the radiative heat transfer between any surface elements of all materials in the directional solidification furnace, a dynamic ray tracing algorithm was developed to simulate the entire process of directional solidification. Then, the simulated results were compared with the theoretical results and experimental results, respectively. Finally, based on the present model and method, the simulation program developed was applied to the directional solidification of actual castings.

1 Model description and numerical method

In the present study, it is assumed that the directional solidification furnace is in a complete vacuum state and the convection of molten metal in the shell is neglected. Two discrete systems for numerical simulation are established. One is the cylindrical coordinate system, which is used to characterize the temperature distribution of the furnace heating zone or cooling zone. The other is the Cartesian coordinate system, which is used to calculate the temperature field of the cluster of blades and other materials. Figure 1 shows the schematic diagram of the directional solidification process. The governing equations and numerical method for calculating the temperature field are described in detail below.

1.1 Transient global temperature calculation

The governing equation for transient global temperature is written as:

$$\rho c_{\mathrm{p}} \frac{\partial T}{\partial t} = k_i \frac{\partial^2 T}{\partial x^2} + k_i \frac{\partial^2 T}{\partial y^2} + k_i \frac{\partial^2 T}{\partial z^2} + \rho L \frac{dF_{\mathrm{S}}}{dT} + Q_{\mathrm{R}} \quad (1)$$

where ρ is density, c_{p} is specific heat, T is temperature, t is time, k_i is thermal conductivity, L is latent heat, F_{S} is solid fraction, and Q_{R} is radiation heat.

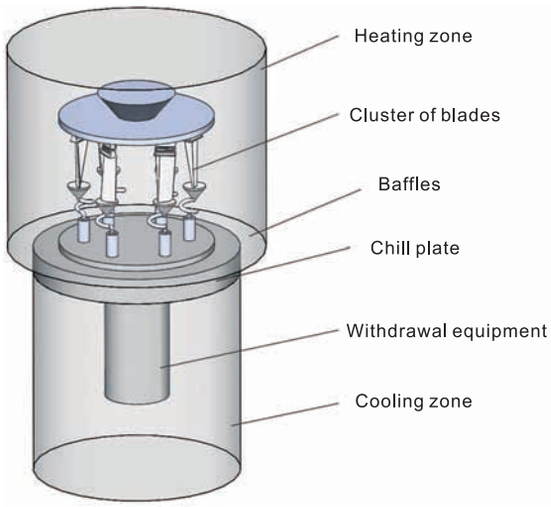

Fig. 1: Schematic diagram of directional solidification process

At the boundary walls between different materials, the heat flux per unit area, q, is given by:

$$q=h(T_A-T_B) \quad (2)$$

where h is the interfacial heat transfer coefficient. T_{A} and T_{B} are the temperatures of two different materials at the boundary walls, respectively.

1.2 Radiant heat calculation based on DTM

Due to the assumption of vacuum in the directional solidification furnace, the transient radiation heat calculations are greatly simplified, considering only the radiative heat transfer between the two surface elements. Accordingly, the 3D Discrete Transfer Method is employed to calculate the radiative heat transfer. Specifically, the upper hemisphere space on arbitrary boundary surface is discretized into a series of spatial solid angles (Ω), which can be defined by the azimuthal angle (β) and the latitudinal angle (θ). A characteristic ray is defined in a spatial solid angle, and all the radiation heat in the spatial solid angle is concentrated on the characteristic ray. Figure 2 shows the schematic diagram of a radiation characteristic ray based on the discrete transfer method.

According to Lambert's law, the radiation heat per unit area $E(\theta, \beta)$ of any surface element varies with orientation in its upper hemisphere space. It can be obtained by:

$$E(\theta, \beta)=I(\theta, \beta)\, d\Omega \cos\theta \quad (3)$$

where $I(\theta, \beta)$ is directional radiation intensity.

The radiometric force of characteristic ray within any spatial solid angle per unit area can be expressed as:

$$E_i(d\theta, d\beta) = \int_{\theta}^{\theta+d\theta} \int_{\beta}^{\beta+d\beta} E(\theta, \beta)\, dA_i \quad (4)$$

where A_i is area. The radiometric force of all characteristic rays (E_N) in the upper hemisphere space of any surface element can be expressed as:

$$E_N = \int_0^{\pi/2} \int_0^{2\pi} E_i(d\theta, d\beta)\, dA_i \quad (5)$$

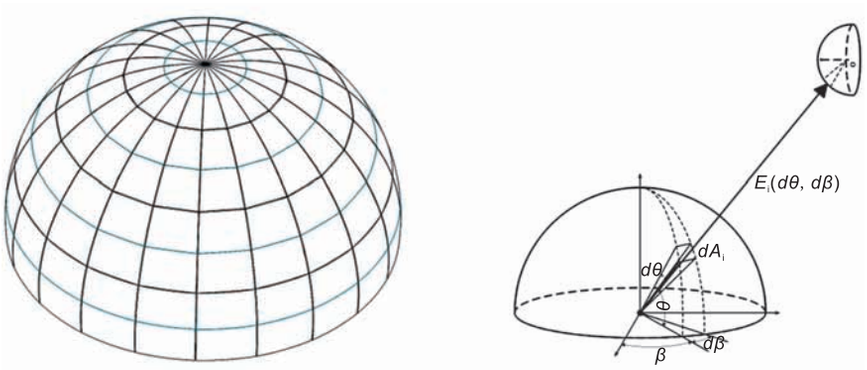

Fig. 2: Schematic diagram of radiation characteristic ray based on discrete transfer method

Then the ratio ($k_{i,j}$) of the radiometric force of a characteristic ray within any spatial solid angle per unit area to the total radiometric force in the upper hemisphere space of the surface element can be given by [11]:

$$k_{i,j} = \frac{E_i\left(d\theta, d\beta\right)}{E_{\mathrm{N}}} = \frac{\Delta\beta}{4\pi}\left[\cos\left(2\theta\right) - \cos\left(2\theta + 2\Delta\theta\right)\right] \quad (6)$$

For the sake of simplicity, the radiation scattering and reflection problems between any two surface elements are neglected. The radiation heat of a characteristic ray within any spatial solid angle per unit area ($q_{1,2}$) can be calculated by:

$$q_{1,2} = k_{i,j}\sigma\left(T_1^4 - T_2^4\right) \Big/ \left(\frac{1-\varepsilon_1}{\varepsilon_1 A_1} + \frac{1-\varepsilon_2}{\varepsilon_2 A_2} + \frac{1}{A_1 X_{1,2}}\right) \quad (7)$$

where T_1, T_2 are respectively the temperatures of the surface elements corresponding to the two spatial solid angles per unit area, ε_1, ε_2 are the emissivities of the surface elements, A_1, A_2 are the areas of the surface elements, $X_{1,2}$ is the view factor of the surface element.

Finally, the radiation heat of any surface element (Φ) can be obtained by summing all the radiation characteristic ray energy in the upper hemisphere space of the surface elements, which is given by:

$$\Phi = \sum_{n=1}^{N} q_{1,2} \quad (8)$$

1.3 Accuracy improvement of radiation numerical calculation based on FDM

Since the radiation heat is transmitted between any two surface elements, it is noted that the surface area of the two elements has an important influence on the numerical calculation of the radiation heat. Figure 3 shows the typical geometric model of regular (cube) and irregular (sphere) surfaces divided by finite difference grids. The total external surface area of a regular surface model divided by finite difference grids is equal to the original total external surface area. And the radiation numerical accuracy of the regular surface model increases with the decrease of mesh size. In contrast, due to the zigzag shape, the total external surface area of an irregular surface model divided by finite difference grids is larger than the original total external surface area. The radiation numerical accuracy of the irregular surface model decreases with the increase of mesh size.

Besides, the accuracy of boundary conditions increases with the decrease of mesh size, which is equally important for the accuracy of numerical calculation. Therefore, a method for improving accuracy of radiation numerical calculation is proposed, as described below.

It is assumed that the radiation heat absorbed by the effective external surface area of a single surface element is proportional to its original total external surface area. The effective external surface area of each surface element is evaluated by the following five conditions, as shown in Fig. 4:

(a) When only one surface of a single surface element is the external surface, the effective external surface area (S_1) is defined as the original area (S_0);

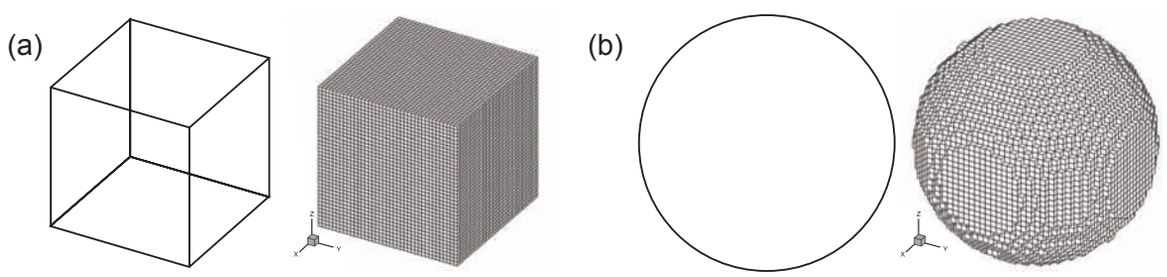

Fig. 3: Schematic diagram of a typical geometric model of regular (cube) (a) and irregular (sphere) (b) surfaces divided by finite difference grids

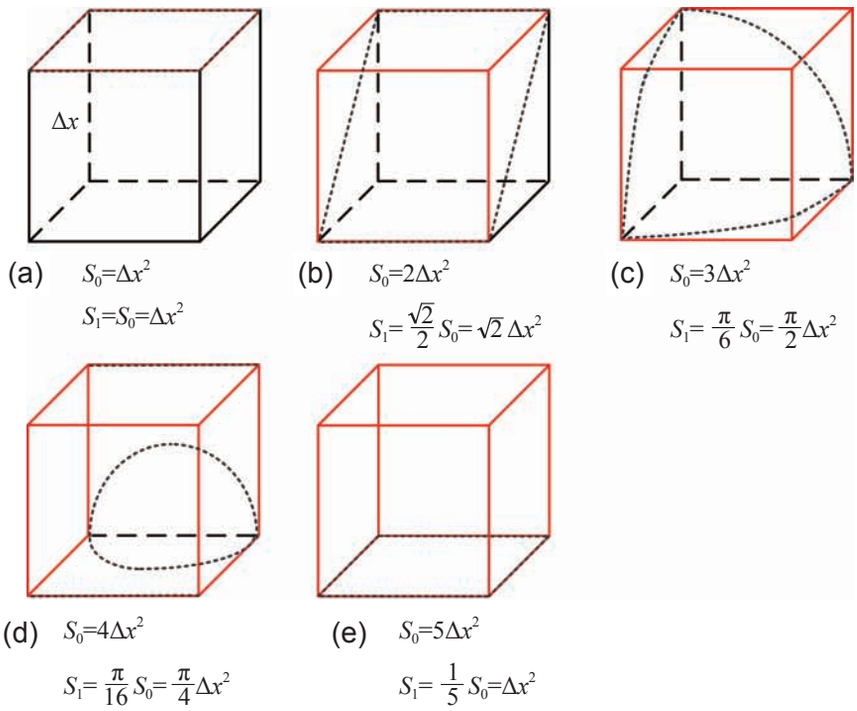

Fig. 4: Schematic diagram of external surface area estimation of a single surface element

(b) When two surfaces of a single surface element are the external surfaces, the effective external surface area (S_1) is defined as $\sqrt{2}\cdot S_0/2$;

(c) When three surfaces of a single surface element are the external surfaces, the effective external surface area (S1) is defined as $\pi\cdot S_0/6$;

(d) When four surfaces of a single surface element are the external surfaces, the effective external surface area (S_1) is defined as $\pi\cdot S_0/16$;

(e) When five surfaces of a single surface element are the external surfaces, the effective external surface area (S_1) is defined as $S_0/5$;

It should also be noted that the actual casting geometry model may be a mixed geometric model of regular and irregular surfaces. The above improved method of radiation numerical calculation can improve the calculation accuracy of the radiation heat transfer of the irregular surface model to some extent, but it will reduce the calculation accuracy for the regular surface geometric model. The overall calculation of the radiation heat transfer is evaluated below.

2 Dynamic ray tracing algorithm

As mentioned above, the radiation heat is calculated by the characteristic ray calculation based on the discrete transfer method, which avoids the calculation of a large number of view factors and thus improves the calculation efficiency. Nevertheless, due to the process conditions of directional solidification, there are still problems with the characteristic ray tracing calculation. Firstly, the casting in the directional solidification process has a relative movement with the furnace heating zone or the cooling zone, so it is necessary to dynamically calculate the radiative heat transfer between any two surface elements. Secondly, the radiant heat transfer occurs not only between the heater and other materials, but also between any two surface elements visible in the field of view. Thirdly, as a characteristic ray is emitted from one surface element in the furnace, it may intersect with multiple surface elements in the ray direction. The key point is to determine the surface element closest to the emitting surface element and evaluate the radiation heat between them.

To solve these problems, a dynamic ray tracing algorithm is developed. Figure 5 presents the schematic diagram of radiative heat transfer during the directional solidification process. A spatial region including all castings, shells and chill plate is defined as the bounding volume. The origin (O)

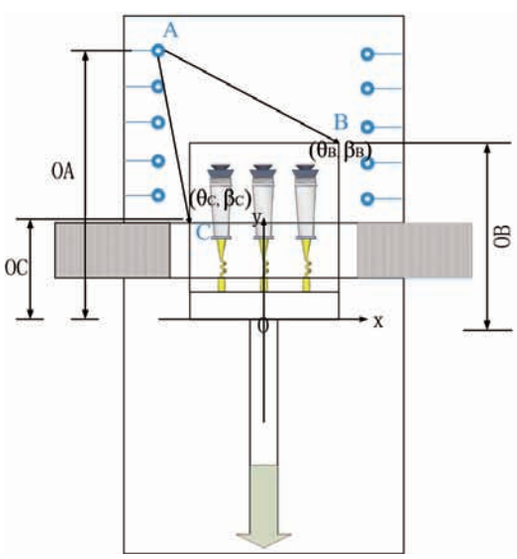

Fig. 5: Schematic diagram of radiative heat transfer during directional solidification process

of the coordinate system is set at the bottom of the bounding volume, which moves with respect to the furnace wall under the pulling action of the withdrawal unit. During the directional solidification process, the y-coordinate of A on the wall of the furnace gradually changes, while the coordinates of B and C on the bounding volume are relatively unchanged. As the azimuthal angle of the radiation characteristics ray of A-B and A-C changes with time, it is necessary to recalculate the radiation heat in each time step. Besides, due to the complex geometric model of the castings, shells, and chill plate in the bounding volume, the characteristic rays must be also accurately traced in the ray direction inside the bounding volume.

The detailed dynamic tracing algorithm is as follows:

(a) Single bounding volume

Since there is only one complex casting system (single bounding volume) in the directional solidification furnace, the characteristic rays emitted from any surface element of the casting system may intersect the surface elements of the casting system itself or the furnace wall. To ensure that no intersection point is missing and to reduce the amount of calculation, an adaptive step length variation method in real-time is used to calculate the cumulative length of the characteristic ray, as shown in Fig. 6. There are two situations discussed here: (a1) when the moving point of the current characteristic ray is inside the bounding volume, the step size of characteristic ray is defined as gird size; (a2) when the moving point of the current characteristic ray is outside the bounding volume and there is no intersection point between the current characteristic ray and the surface element of the casting system itself, the step size of characteristic ray is defined as the linear length between the moving point of the current characteristic ray and the surface element of the furnace wall. That is to say, the characteristic ray will directly intersect the surface element of the furnace wall, such as *A*, *B*.

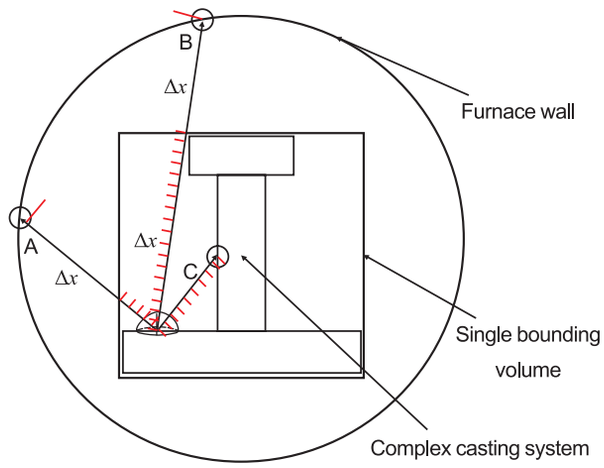

Fig. 6: Schematic diagram of radiative heat transfer during directional solidification process

(b) Multiple bounding volumes

When there are many complex casting systems in the directional solidification furnace, each complex casting system is defined as a bounding volume. Then, the characteristic rays emitted from any boundary surface may intersect with the surface elements such as the boundary surface of any one or more complex casting systems, the casting system itself and the furnace wall, respectively. This will result in a more complicated process of characteristic ray tracing. The schematic diagram of adaptive step length variation method for multiple bounding volumes is presented in Fig. 7.

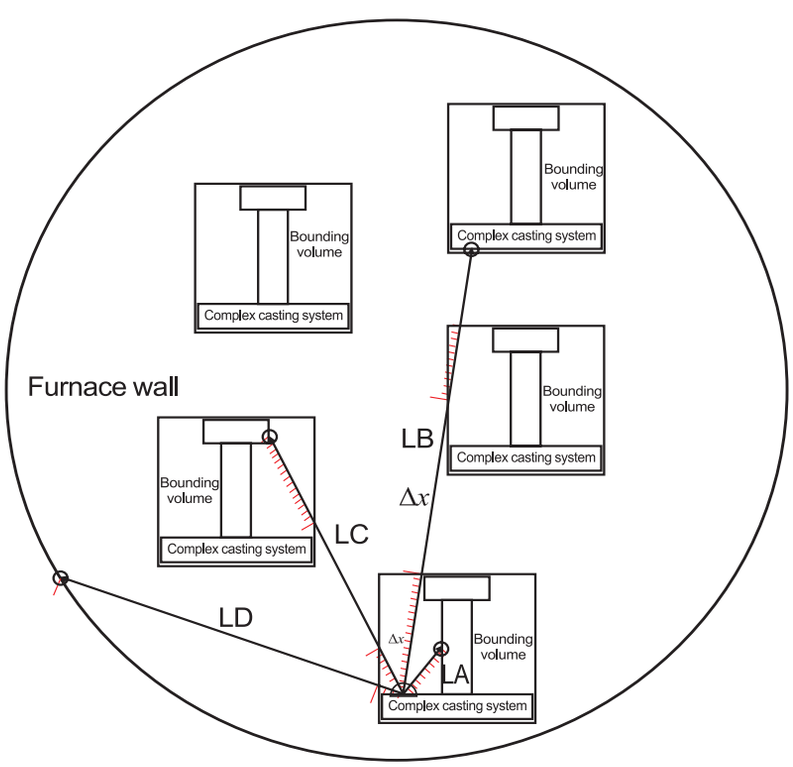

Fig. 7: Schematic diagram of adaptive step length variation method for multiple bounding volumes

In the first step, a number of characteristic rays are emitted from any boundary surface of the surface element in the bounding volume. The length of characteristic ray is cumulatively increased at the same grid step size, thus avoiding missing the intersection of the characteristic ray (LA) with the surface element of the casting system itself. In the second step, when the characteristic ray does not intersect with the surface element of the casting system itself, after leaving the bounding volume itself, it is necessary to check whether the characteristic ray intersects with another bounding volume or the furnace wall. If there is an intersection at this time along the ray direction, the step size of characteristic ray is defined as the linear length between the bounding volume and the other adjacent bounding volume or the surface element of the furnace wall. In the third step, when the current characteristic ray intersects with any other bounding volume along the ray direction, the step size of the characteristic ray is redefined as the grid size. It is determined whether the current characteristic ray intersects with the surface element of the casting system in this bounding volume. If not, the first and second steps mentioned above are repeated, such as characteristic ray LB. Otherwise, tracking is stopped, such as characteristic ray LC. Likewise, when the current characteristic ray does not intersect with any other bounding volume, it means that there is no intersection between the current characteristic ray and any other casting systems. Then the current characteristic ray will directly intersect with the surface element of the furnace wall. After the current characteristic ray is cumulatively increased, the characteristic rays cease to be tracked, such as characteristic ray LD.

3 Results and discussion

3.1 Comparison with theoretical solution of radiative heat transfer

To evaluate the feasibility of the radiative heat transfer model and algorithm in this study, the radiation numerical results of a closed system consisting of two blackbodies are compared with those calculated by Stefan-Boltzman law. The original solution refers to the result of no differential mesh correction, and the modified solution refers to the result of the differential mesh correction. It is assumed that this surface closed system consists of the outer surface of the furnace heating (1,773.15 K) and the outer surface of the casting system (298.15 K), in which the outer surface of the casting system is assumed to be a typical geometric model of regular (cube, the length of a side is 0.2 m) or irregular (sphere, the diameter is 0.2 m) surface. Figure 8 shows the change in radiation energy as a function of mesh size.

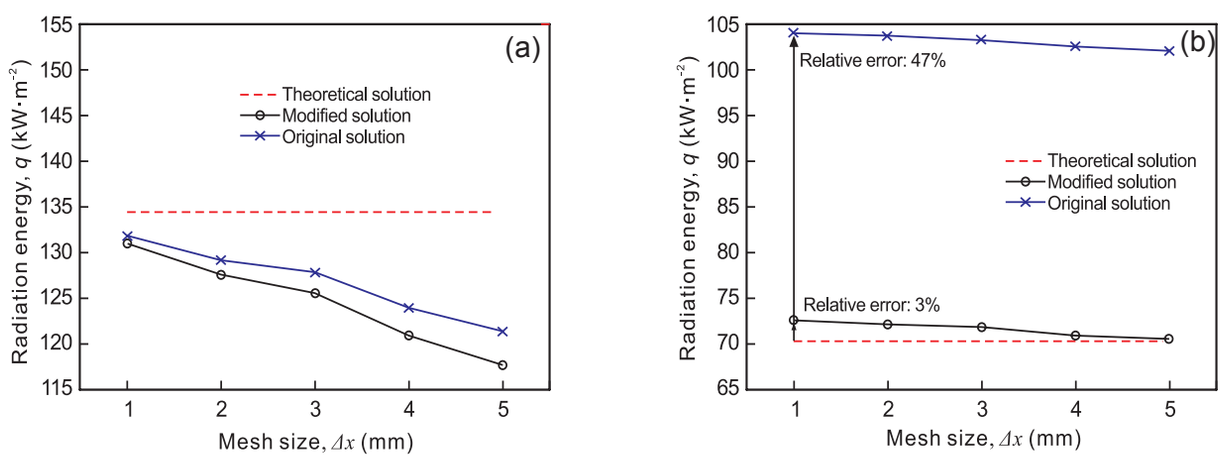

Fig. 8: Radiation energy as a function of mesh size: (a) Regular surface (cube); (b) Irregular surface (sphere)

For the radiative heat transfer on regular surfaces, the numerical results of the radiation energy decrease gradually with the increase of the mesh size and deviate from the theoretical solution. This shows that the accuracy of numerical calculation decreases with the increase of mesh size, and the accuracy of the numerical results calculated by using of the numerical improvement method in this present study is slightly lower than that of the original solution. For the radiative heat transfer on irregular surfaces, with the increase of the mesh size, the numerical results of the radiation energy gradually decrease and approach the theoretical solution. The accuracy of the numerical results calculated by using of the numerical improvement method is greatly improved over that of the original solution. Although the accuracy of all the numerical results gradually increased, the difference between the original solution and the theoretical solution reached 47% and the difference between the modified solution and the theoretical solution is only 3%. The simulation results show that the surface area of the geometric model has an important influence on the radiative heat transfer. In addition, it can be seen that with respect to the accuracy reduction of the numerical calculation of the radiative heat transfer on the regular surface, the numerical improvement method can greatly improve the accuracy of the numerical calculation of the radiative heat transfer on the geometric model composed of regular and irregular surfaces to a certain extent.

3.2 Comparison with experimental results during directional solidification

To validate the effectiveness of the radiative heat transfer model and algorithm, a directional solidification experiment at the

withdrawal rate of 6 mm·min^{-1} is performed on the plate-castings with size similar to that of the blades.

Considering the impact of molten metal on the casting process, the thermocouple wire is protected by a corundum ceramic tube with a diameter of 4 mm. The geometric model, thermocouple assembly and temperature measuring point P on the casting are shown in Fig. 9. The alloy material is the nickel-based superalloy whose chemical composition is Ni-7.82Cr-5.34Co-2.25Mo-4.88W-6.02Al-1.94Ti-3.49Ta (wt.%). The thermophysical parameters of the alloy calculated by JMatPro software vary with temperature, in which the liquidus temperature and solidus temperature are 1,643.0 K and 1,598.3 K, respectively. The latent heat of the alloy is 233,371.59 J·kg^{-1}. The other key simulation parameters are listed in Table 1.

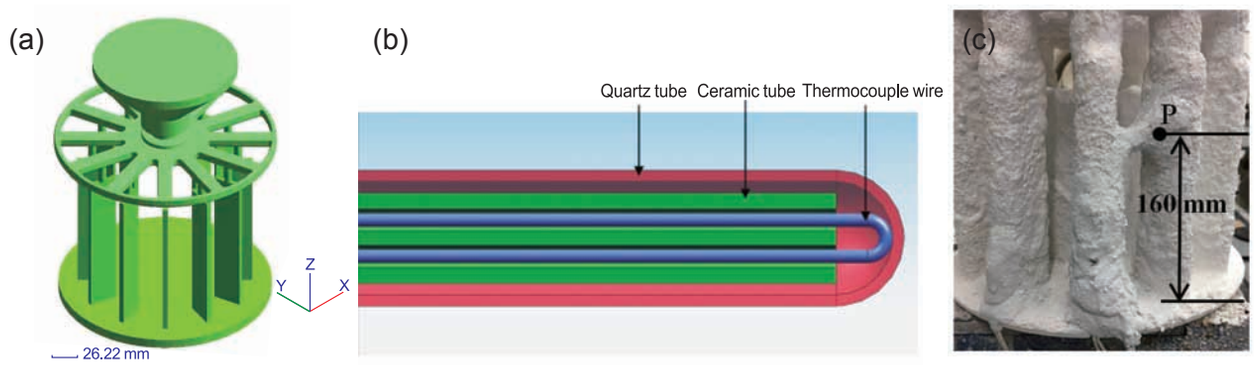

Fig. 9: Gometric model (a), thermocouple assembly (b) and temperature measuring point P (c)

Table 1: Key simulation parameters

Parameters	Values
Temperature of heating zone (K)	1,798.15
Temperature of cooling water (K)	298.15
Withdrawal rate (mm·min^{-1})	6
Emissivity of heating zone	0.8
Emissivity of other materials	0.4
Shell density (kg·m^{-3})	2,731
Chill plate density (kg·m^{-3})	8,461
Specific heat of shell (J·kg^{-1}·K^{-1})	800
Specific heat of chill plate (J·kg^{-1}·K^{-1})	382
Thermal conductivity of shell (W·m^{-1}·K^{-1})	4.2
Thermal conductivity of chill plate (W·m^{-1}·K^{-1})	426
Heat transfer coefficient between shell and casting (W·m^{-2}·K^{-1})	900
Heat transfer coefficient between chill plate and casting (W·m^{-2}·K^{-1})	2,400
Heat transfer coefficient between chill plate and shell (W·m^{-2}·K^{-1})	1,000
Heat transfer coefficient between chill plate and cooling water (W·m^{-2}·K^{-1})	2,500

Figure 10 presents the P-point cooling curves obtained by experimental measurement and numerical calculation, respectively. As shown, the temperature of the P-point in the casting remained almost unchanged in the early stage, then decreased rapidly and finally decreased slowly. It can be seen that the agreement between the experimental results and numerical results is good, although there is a slight deviation in the middle of the cooling curve.

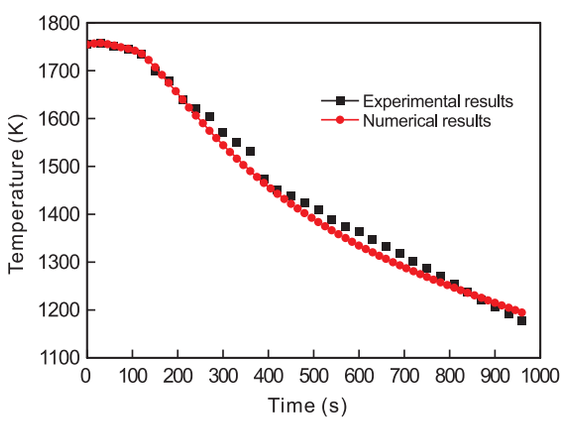

Fig. 10: P-point cooling curves obtained by experimental measurement and numerical calculation

3.3 Applications for complex multiple turbine blades in directional solidification process

Generally, the directional solidification process mainly includes shell preheating, pouring of molten metal and casting solidification. The computation domain is divided into uniform cubic cells 195×195×195 in the three dimensions. The mesh size is 1.1×10^{-3} m. Figure 11 presents the casting geometric model of complex multiple turbine blades and the mesh model divided by finite difference grids.

(1) Shell preheating

Figure 12 shows the temperature field of the shell under different viewing angles at t=3,000 s. In view of the overall situation, the maximum temperature difference of the shell is located in the region between the chill plate and starter block.

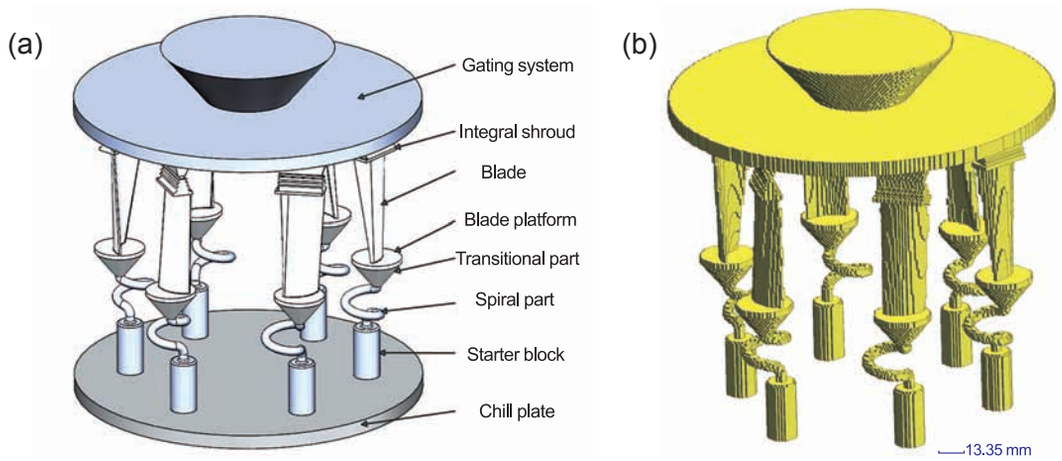

Fig. 11: Casting geometric model of complex multiple turbine blades (a) and mesh model divided by finite difference grids (b)

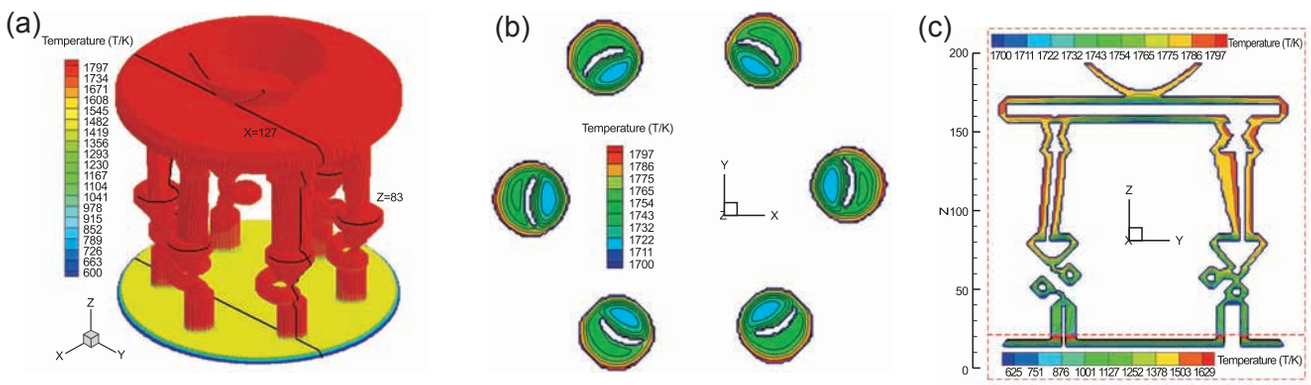

Fig. 12: Temperature field of shell under different viewing angles at *t*=3,000 s: (a) Temperature field of shell; (b) Temperature field at cross-section of *Z*=83; (c) Temperature field at cross-section of *X*=127

Above the starter block, the temperature of all parts of the shell are approximately close to the maximum temperature of the given heating process curve and their respective temperature differences are small. At the cross-section of X=127, the temperature ranges from 1,700 K to 1,797 K, and the average temperature gradient calculated is 519 K·m^{-1}. Below the starter block, there is a significant difference in temperature at a smaller distance. The temperature ranges from 625 K to 1,629 K, and the average temperature gradient calculated is 10,141 K·m^{-1}. It can be noted from the profile analysis that the temperature field of the shell is symmetrically distributed in the center at the cross-section of Z=83, and the temperature of the external surface of the shell radially outward is always greater than the temperature of the internal surface in the radial direction of the shell, which is consistent with the previous results.

(2) Casting solidification

Subsequently, the pouring process of the molten metal is carried out. Since the filling time is relatively short, it is assumed that the molten metal is instantaneously poured. Under the temperature field of above shell, (especially under the high temperature gradient between the chill plate and starter block,) the molten metal rapidly solidifies. Figure 13 shows the temperature field of the cluster of blades during directional solidification.

As shown in Fig.13, with the dynamic movement of the cluster of blades, the starter block, spiral part, blades and gating system begin to solidify along the positive direction of Z axis in sequence. It can be observed that the temperature distribution on the external surface of the shell is obviously uneven. To further study the temperature variation in the directional solidification process, a single blade is selected from the complex multiple turbine blades. The temperature of the key parts of the single blade, such as the starter block A (35, 91, 27), the spiral part B (27, 100, 51), the transitional part C (30, 95, 73), the blade platform D (28, 95, 80), the blade E (29, 95, 113), the integral shroud F (32, 95, 143), and the gating system G (30, 95, 163) are chosen, and their respective temperature curves with time are shown in Fig. 14.

As shown in Fig.14, with the dynamic movement of the cluster of blades, the key parts of A, B, C, D, E, F, and G are cooled down in sequence. At the time t=10 s, the cooling rate of part A reaches the maximum value (5.03 K·s^{-1}), and then it gradually decreases. At the time t=200 s, the cooling rate of part B increases first and reaches the maximum value (1.87 K·s^{-1}), and then also gradually decreases. Likewise, this is followed by parts of C, D, E, F, and G. In addition, it can be seen that the maximum cooling rate of the blade including the key parts of A,

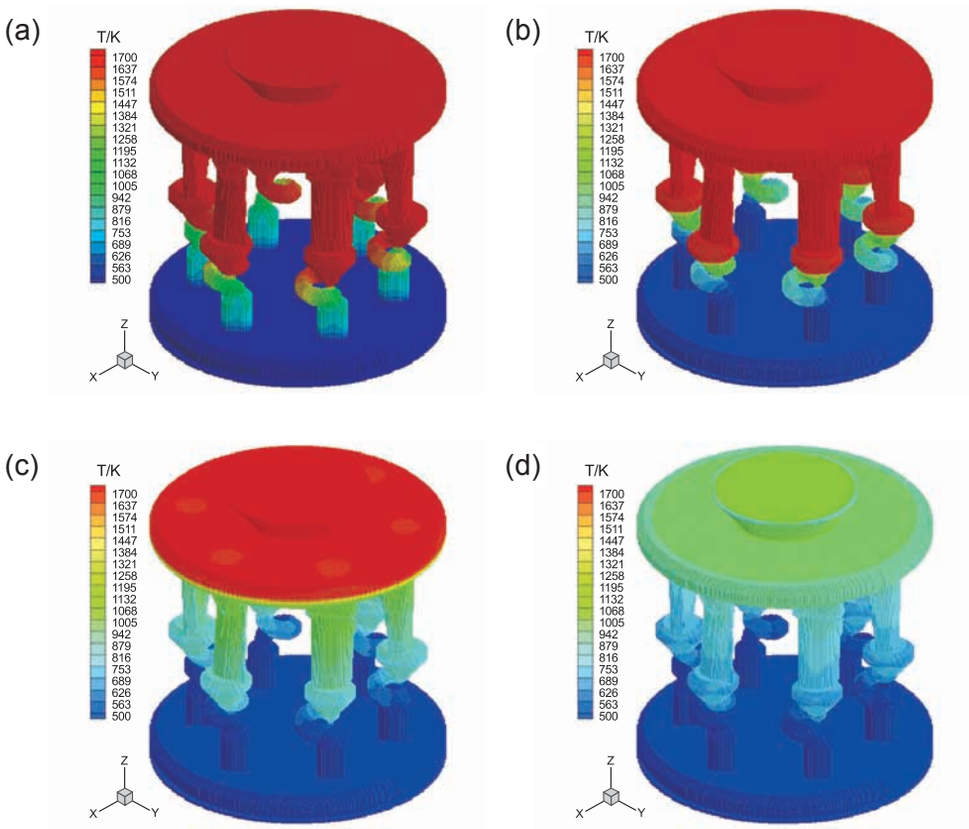

Fig. 13: Temperature fields of cluster of blades during directional solidification: (a) *t*=500 s; (b) *t*=1,000 s; (c) *t*=2,000 s; (d) *t*=3,000 s

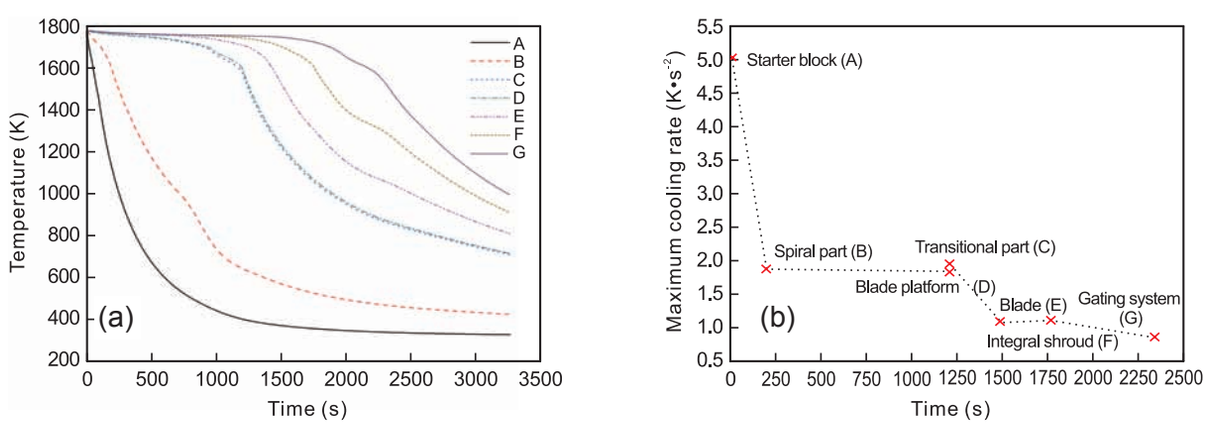

Fig. 14: Time history of temperature for a single blade: (a) Temperature vary with time; (b) Maximum cooling rate vary with time

B, C, D, E, F, and G decreases gradually. The minimum of the maximum cooling rates is located in the gating system of the blade, with a size of 0.85 K·s^{-1}.

In order to avoid the formation of unfavorably oriented grain and misoriented grain, the solid-liquid interface of the molten alloy should be kept as horizontal as possible during directional solidification. That is to say, the temperature difference of the horizontal plane (XOY) along the positive direction of Z-axis should be reduced as much as possible. Accordingly, the temperature difference of the key parts of blade is analyzed along the radial position. The nodal coordinates along different radial positions of each key part are listed in Table 2.

Figure 15 presents the time history of the maximum temperature difference for the key parts of blade. It can be noted that the maximum temperature difference of the part D along the radial position is the largest of all the parts, (18.481 K at *t*=1,250 s), which is more likely to lead to the generation of unfavorably oriented grain and misoriented grain. In contrast, it is difficult to form the unfavorably oriented grain and misoriented grain in part E, which reaches the maximum value of 0.427 K at time of *t*=1,710 s.

Table 2: Coordinate values of internal surface points, interior points and external surface points of blade

Key part	Points of internal surface	Interior points	Points of external surface
A	(42, 91, 27)	(35, 91, 27)	(30, 91, 27)
B	(29, 100, 51)	(27, 100, 51)	(26, 100, 51)
C	(38, 95, 73)	(30, 95, 73)	(22, 95, 73)
D	(43, 95, 80)	(28, 95, 80)	(17, 95, 80)
E	(31, 95, 113)	(29, 95, 113)	(28, 95, 113)
F	(35, 95, 143)	(32, 95, 143)	(30, 95, 143)

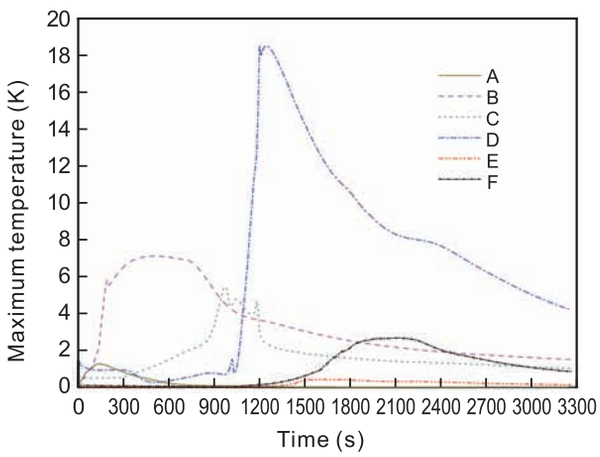

Fig. 15: Time history of maximum temperature difference for key parts of blade

4 Conclusions

A 3D transient global heat transfer model of directional solidification by the Bridgman method based on FDM is developed. In this model, the radiation heat is calculated by the DTM. An external surface area modified method for irregular geometric models is proposed to reduce the zigzag shape caused by finite difference grids. Considering the radiative heat transfer between any surface elements of all materials in the directional solidification furnace, a dynamic ray tracing algorithm is developed to simulate the entire process of directional solidification. Then, the simulated results are compared with the theoretical results and experimental results, respectively. It is inferred that the developed model is effective and practical, and the modified method for external surface area can greatly improve the accuracy of the numerical calculation of the radiative heat transfer on the geometric model composed of regular and irregular surfaces to a certain extent. The numerical simulation program developed in this study based on the developed model and method can be applied to simulate the directional solidification process for complex multiple turbine blades of Ni-based superalloys effectively.

References

[1] Rezaei M, Kermanpur A, Sadeghi F. Effects of withdrawal rate and starter block size on crystal orientation of a single crystal Ni-based superalloy. J. Cryst. Growth, 2018, 485: 19–27.
[2] Wang F, Ma D, Zhang J, et al. Effect of solidification parameters on the microstructures of superalloy CMSX-6 formed during the downward directional solidification process. J. Cryst. Growth, 2014, 389: 47–54.
[3] Szeliga D, Kubiak K, Sieniawski J. Control of liquidus isotherm shape during solidification of Ni-based superalloy of single crystal platforms. J. Mater. Process Technol., 2016, 234: 18–26.
[4] Lian Y, Li D, Zhang K. Effects of the location of a cast in the furnace on flatness of the solidification front in directional solidification. J. Cryst. Growth, 2016, 451: 33–41.
[5] Thomas B G, Goettsch D D. Modeling the directional solidification process. In: Proc. the 5th International Conference on Modeling of Casting, Welding and Advanced Solidification Processes (MCWASP), edited by Rappaz M, Ozgu M R, Mahin K W. The Minerals, Metals and Materials Society, 1991.
[6] Galantucci L M, Tricarico L. A computer-aided approach for the simulation of the directional-solidification process for gas turbine blades. J. Mater. Process. Technol., 1998, 77: 160–164.
[7] Elliott A J, Pollock T M. Thermal analysis of the Bridgman and Liquid-Metal-Cooled directional solidification investment casting processes. Metall. Mater. Trans. A, 2007, 38: 871–882.
[8] Miller J D. Heat extraction and dendritic growth during directional solidification of single-crystal nickel-base superalloys. University of Michigan, M1-Doctor, 2011.
[9] Yu J, Xu Q Y, Cui K, et al. Numerical simulation of solidification process on single crystal Ni-based superalloy investment castings. J. Mater. Sci. Technol., 2007, 23: 47–54.
[10] Yan X W, Zhang H, Tang N, et al. Multi-scale simulation of single crystal hollow turbine blade manufactured by liquid metal cooling process. Prog. Nat. Sci. Mater. Int., 2018, 28: 78–84.
[11] Pan D, Xu Q Y, Liu B C. Modeling on directional solidification of superalloy blades with furnace wall temperature evolution. Acta Metall. Sin., 2010: 294–303.

This research was financially supported by the National Nature Science Fund Projects of China (Nos. 51475181 and 51605174).